

Possible metallization of the Mott insulators TiOCl and TiOBr: effects of doping and external pressure

Christine A. Kuntscher, Matthias Klemm, Siegfried R. Horn, Michael Sing, Ralph Claessen

Angaben zur Veröffentlichung / Publication details:

Kuntscher, Christine A., Matthias Klemm, Siegfried R. Horn, Michael Sing, and Ralph Claessen. 2009. "Possible metallization of the Mott insulators TiOCl and TiOBr: effects of doping and external pressure." *The European Physical Journal Special Topics* 180 (1): 29–42. <https://doi.org/10.1140/epjst/e2010-01210-7>.

Nutzungsbedingungen / Terms of use:

licgercopyright

Dieses Dokument wird unter folgenden Bedingungen zur Verfügung gestellt: / This document is made available under these conditions:

Deutsches Urheberrecht

Weitere Informationen finden Sie unter: / For more information see:

<https://www.uni-augsburg.de/de/organisation/bibliothek/publizieren-zitieren-archivieren/publiz/>



Possible metallization of the Mott insulators TiOCl and TiOBr: Effects of doping and external pressure

C.A. Kuntscher^{1,a}, M. Klemm¹, S. Horn¹, M. Sing², and R. Claessen²

¹ Experimentalphysik 2, Universität Augsburg, 86135 Augsburg, Germany

² Experimentelle Physik 4, Universität Würzburg, 97074 Würzburg, Germany

Abstract. We report the results of doping- and pressure-dependent experimental investigations on the low-dimensional Mott-Hubbard insulators TiOCl and TiOBr. As observed by photoelectron spectroscopy, doping with Na and K shifts the valence band to higher binding energies associated with a jump of the chemical potential. With increasing doping, a broad hump develops close to the Fermi energy and the energy gap “softens”. The application of pressure induces the appearance of spectral weight close to the Fermi energy, as probed by infrared transmittance and reflectance measurements. The pressure-induced changes in the electronic properties coincide with a structural phase transition according to powder X-ray diffraction studies under pressure. The experimental findings are compared to theoretical predictions.

1 Introduction

There are two possibilities to drive a weakly interacting, metallic electron system into an insulating state. In Mott insulators, electron correlations induce a charge gap in the excitation spectrum for partially occupied bands with integer filling [1], while in Anderson insulators a locally varying disorder potential leads to localization at arbitrary band-filling [2]. In real materials like transition metal oxides, both electronic correlations and disorder often coexist and may be of comparable strength. In such cases, new types of insulating phases can occur which are qualitatively different from the simple Mott and Anderson insulators [3].

Starting reversely from a Mott insulator, a metal-insulator transition (MIT) can be induced by either changing the bandfilling n (“filling-controlled MIT” – FC-MIT) or the bandwidth (“bandwidth-controlled MIT” – BC-MIT). The latter is determined by the ratio U/t , where U denotes the on-site Coulomb repulsion and t the hopping integral of the charge carriers. These two possible routes of an MIT are indicated in the metal-insulator phase diagram (Fig. 1(a)) based on the Hubbard model, according to Ref. [4]. The vertical axis is located at $n = 1$, which corresponds to the half-filled case. Experimentally, the band-filling can be varied either by chemical substitution or by intercalation of suitable acceptors or donators. The bandwidth can be controlled via chemical or external pressure, the latter acting on the parameter t in a direct and clean way, i.e., without introducing disorder.

There are several prominent examples of extensive studies of the MIT [4]. Prototypical examples of the Mott MIT induced by application of pressure or by chemical substitution are V_2O_3 and $NiS_{2-x}Se_x$. The filling-controlled MIT was demonstrated for the series $R_{1-x}A_xTiO_3$ with R being a trivalent rare-earth and A a divalent alkaline-earth ion. Probably the most prominent examples of the filling-controlled MIT are the copper oxide high-temperature

^a e-mail: christine.kuntscher@physik.uni-augsburg.de

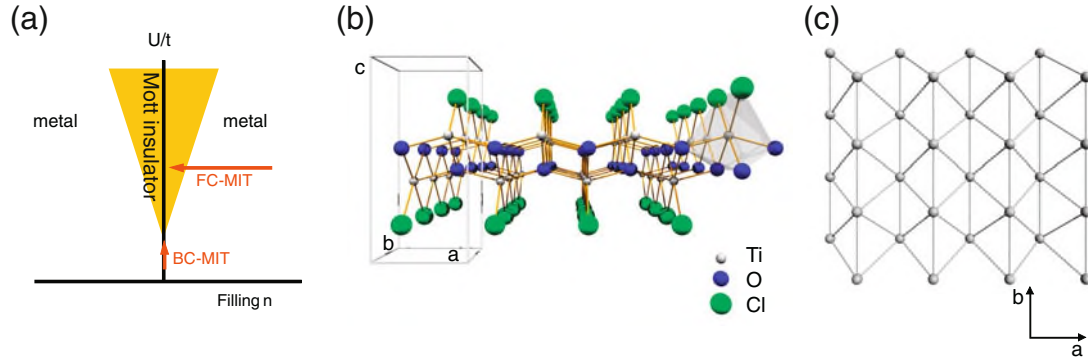


Fig. 1. (a) Metal-insulator phase diagram based on the Hubbard model as a function of the band-filling n and U/t ratio, where U denotes the on-site Coulomb repulsion and t the hopping integral of the charge carriers [4]. The two possible routes for the MIT are the filling-controlled MIT (FC-MIT) and the bandwidth-controlled MIT (BC-MIT). The vertical axis is located at $n = 1$, which corresponds to the half-filled case. The yellow area is in principle metallic, but the charge carriers become easily localized under the strong influence of the MIT due to extrinsic forces such as disorder and electron-lattice coupling. (b) Central projection view of the crystal structure of TiOCl along the b -axis. (c) Triangular Ti mesh of TiOCl, projected along the c -axis. t' denotes the interchain hopping integral.

superconductors. Here superconductivity is achieved by carrier doping of the parent compounds which are antiferromagnetic Mott (or charge-transfer) insulators.

In this paper we report on spectroscopic investigations of the effects of doping and external pressure on the electronic structure of the oxyhalides TiOCl and TiOBr, which are prototypical Mott insulators at room temperature, in order to study the FC- and BC-MIT.

TiOCl(Br) crystallizes in an orthorhombic quasi-two-dimensional structure of the FeOCl type, where buckled bilayers of Ti-O are separated by Cl(Br) ions [5]. The bilayers, which are stacked along the crystallographic c -axis, only weakly interact through van der Waals forces (cf. Fig. 1(b)). Magnetically, spin 1/2 Heisenberg chains form along the crystallographic b axis, mediated by direct exchange ($J = 660$ K and $J = 375$ K for TiOCl and TiOBr, respectively) of the $\text{Ti } 3d_{xy}$ orbitals as evidenced by the observation of a Bonner-Fisher-type magnetic susceptibility at high temperatures and inferred from LDA+U calculations of the electronic structure [6, 7]. Nonetheless, if one projects the Ti sites of one bilayer onto the (a, b) plane one recognizes the triangular arrangement of Ti ions between neighboring chains (cf. Fig. 1(c)) with the inherent possibility of geometrical frustration of the magnetic interactions *across* the chains. These criteria – low dimensionality, spin 1/2, magnetic frustration – make TiOCl(Br) candidates for the realization of a resonating valence bond state [8], which, if doped, could result in exotic superconductivity as has been speculated in the early nineties [9].

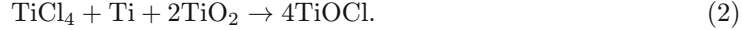
2 Sample preparation and characterization

Single crystals of TiOCl were grown by the chemical vapour transport method [10, 11]. A closed quartz tube is brought into a temperature gradient with the reactants at the hot end. TiOCl single crystals will then grow at the colder end of the quartz tube. The transport is governed by thermal convection. This is aided by a slight inclination of the quartz ampoule. The temperature gradient and the concentrations have to be chosen such that many single crystals of high quality can be obtained. Based on the procedure described by Schäfer et al. [5], the parameters were optimized. First TiOCl was synthesized from TiCl_3 and TiO_2 according to the reaction equation



The experience was often made that the TiOCl crystals were wetted with a thin film of TiCl_4 . At the first contact with air this film heavily reacted and thus spoiled the surface of the TiOCl crystals.

Therefore we tried another route of preparation using TiCl_4 instead of TiCl_3 as the starting material:



It was found that better results could be achieved, with the constraint that the liquid TiCl_4 is more complicated to handle than the TiCl_3 powder. A slight deviation of -5% to -10% of the TiCl_4 mass from the stoichiometric value was used in order to improve the crystal quality.

Quartz ampoules were degassed for several hours at 1000°C . They were then filled with the reactants in an argon glove box and sealed under vacuum ($p < 10^{-4}$ mbar). The ampoules were then exposed to a temperature of 800°C in a ten-zone furnace for several hours, while keeping the dissolution region at a temperature of 450°C , because of cleaning the tube walls. This treatment was followed by a phase where the direction of the temperature gradient was repeatedly switched forth and back. Periods with a “forward” temperature gradient of 650°C at the dissolution zone to 550°C at the growth zone were followed by an inverse “backward” temperature gradient at a lower base temperature. The aim was to dissolve the smallest of the developing crystals in each cycle, so that only the larger ones survive. This is followed by a stage of transport with a “forward” temperature gradient of approximately two weeks. Before the ampoules are taken out of the furnace, the gradient is switched again to the “backward” direction, so that remaining reactants in the gas phase condense in the dissolution zone.

The TiOCl crystals were characterized with various experimental techniques, of which X-ray diffraction, scanning electron microscopy (SEM), and energy dispersive x-ray analysis (EDX) will only be listed. Laue diffraction is a very helpful method to judge the crystal quality of TiOCl crystals. From the Laue pattern the orientation of the crystal can be deduced. Often the crystals possess a needle-like shape, with the longer axis being the b direction. Another indicator of the crystal orientation is the texturing of the surface parallel to the b axis that is frequently observed. Furthermore, the high quality of the TiOCl crystals was demonstrated by measurements of the magnetic susceptibility.

The TiOBr samples were by courtesy supplied by S. van Smaalen (University of Bayreuth) and also grown at the University of Würzburg. They were synthesized in an analogous manner as TiOCl (see Ref. [12] for details).

3 Experiment

For the measurements using photoelectron spectroscopy (PES), clean surfaces were exposed by *in situ* cleavage with scotch tape and subsequently dosed by alkali-metal vapor from SAES dispensers. Spectra were taken using a SPECS PHOIBOS 100 analyzer with a total energy resolution of 700 meV and 70 meV employing Al K_α (1486.6 eV) and He I_α (21.22 eV) radiation for core-level (XPS) and valence-band (UPS) spectroscopy, respectively. The samples were held at elevated temperatures (≈ 360 K) during dosing and measurements to reduce charging and ease alkali-metal diffusion.

Pressure-dependent transmittance and reflectance experiments were conducted at room temperature and for the polarization directions $\mathbf{E}||a, b$ using a Bruker IFS 66v/S FT-IR spectrometer with an infrared microscope (Bruker IRscope II). For the generation of pressure we used a Syassen-Holzapfel diamond anvil cell (DAC) [13] equipped with type IIA diamonds suitable for infrared measurements. For each transmittance and reflectance measurement a small piece (about $80\ \mu\text{m} \times 80\ \mu\text{m}$) was cut from single crystals with a thickness of $\leq 5\ \mu\text{m}$ and placed in the hole of a steel gasket. The pressure was determined by the ruby luminescence method [14].

For the transmittance measurements several pressure transmitting media were used (CsI, methanol : ethanol (4 : 1)-mixture, argon); this leads to small differences in the observed values of the critical pressure of the phase transition, in agreement with other reports [15,16]. The pressure-dependent transmittance was studied in a wide frequency range ($2000\text{--}22000\ \text{cm}^{-1}$) for the polarization directions $\mathbf{E}||a, b$. We measured the intensity $I_s(\omega)$ of the radiation transmitting the sample (see Fig. 2(a)); as reference, for each pressure we focused the incident radiation spot on the empty space in the gasket hole next to the sample and obtained the transmitted intensity $I_r(\omega)$. The ratio $T(\omega) = I_s(\omega)/I_r(\omega)$ is a measure of the transmittance of the sample.

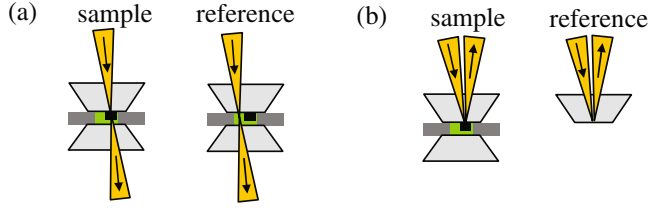


Fig. 2. Geometry for high-pressure (a) transmittance and (b) reflectance measurements of the sample in the diamond anvil cell.

For the reflectance measurements finely ground CsI powder was used as pressure transmitting medium to ensure direct contact of the sample with the diamond window. Pressure-dependent reflectance measurements were carried out in the mid- and nearinfrared frequency range using conventional radiation sources (globar, tungsten source). For TiOBr additional reflectance measurements were conducted in the far-infrared range at the infrared beamline of the synchrotron radiation source ANKA. Reflectance spectra, R_{s-d} , of the sample with respect to diamond were obtained by measuring the intensity $I_{s-dia}(\omega)$ reflected at the interface between the sample and the diamond anvil (see Fig. 2(b)). As reference, the intensity $I_{dia}(\omega)$ reflected from the inner diamond-air interface of the empty DAC was used. The reflectance spectra were calculated according to $R_{s-d}(\omega) = R_{dia} \cdot I_{s-dia}(\omega) / I_{dia}(\omega)$, where R_{dia} was estimated from the refractive index of diamond n_{dia} to 0.167 and assumed to be independent of pressure [17, 18]. The high-pressure ($p > 10$ GPa) reflectance spectra R_{s-d} were fitted with the Drude-Lorentz model combined with the normal-incidence Fresnel equation, taking into account the diamond-sample interface:

$$R_{s-d} = \left| \frac{n_{dia} - \sqrt{\epsilon_s}}{n_{dia} + \sqrt{\epsilon_s}} \right|^2, \quad \epsilon_s = \epsilon_\infty + \frac{i\sigma}{\epsilon_0\omega}, \quad (3)$$

where ϵ_s is the complex dielectric function of the sample and ϵ_∞ is the background dielectric constant. From the function $\epsilon_s(\omega)$ the real part of the optical conductivity, $\sigma_1(\omega)$, can be calculated, which directly shows the excitations in the material.

Pressure-dependent X-ray powder diffraction measurements at room temperature were carried out with monochromatic radiation ($\lambda = 0.4128$ Å) at beamline ID09A of the European Synchrotron Radiation Facility at Grenoble. Crystals were gently ground and placed into a DAC. The applied pressures p were determined with the ruby luminescence method [14]. Helium served as hydrostatic pressure-transmitting medium. Diffraction patterns were recorded with an image plate detector and then integrated with FIT2D [19] to yield intensity vs 2θ diagrams. The DAC was rotated by $\pm 3^\circ$ during the exposure to improve the powder averaging. We carried out LeBail fits of the diffraction data using the Jana2006 software [20], in order to determine the lattice parameters as a function of pressure.

4 Results and discussion

4.1 Effects of doping

As pointed out above the Cl(Br) sandwiched Ti-O bilayers of TiOCl(Br), which are stacked along the c axis, are only coupled via van der Waals forces and thus have enough space in between to accommodate donor or acceptor atoms or even molecules [21]. Usually, these are intercalated using wet chemistry [21]. Alternatively, it has been recently demonstrated that electron doping can be achieved at the surface of $\text{YBa}_2\text{Cu}_3\text{O}_{7-\delta}$ by the evaporation of alkali-metal atoms [22]. The latter route we followed using Na and K to investigate the changes in the electronic structure upon doping by PES (within the scope of this paper TiOCl and TiOBr as well as Na and K are interchangeable). Doing so one has to ensure that (i) the alkali-metal atoms really donate their outer electrons to the Ti $3d$ states of the host crystal (i.e., do not just

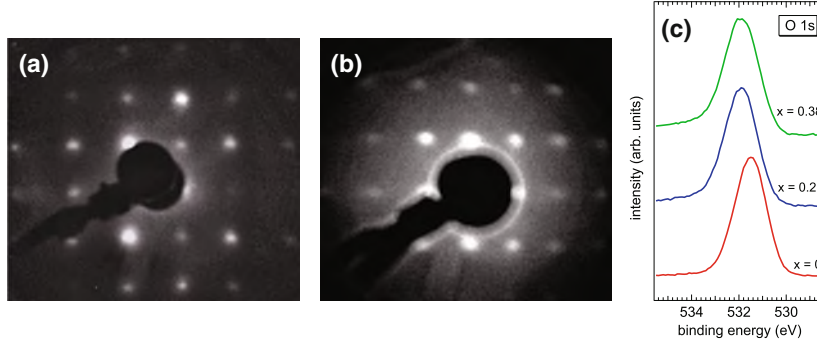


Fig. 3. (a) LEED pattern of a pristine TiOCl cleavage surface ($E = 130$ eV). (b) LEED pattern of the same surface as in (a) after Na dosing ($E = 160$ eV), corresponding to a doping concentration $x \approx 0.2$. (c) $O 1s$ spectra for various doping concentrations.

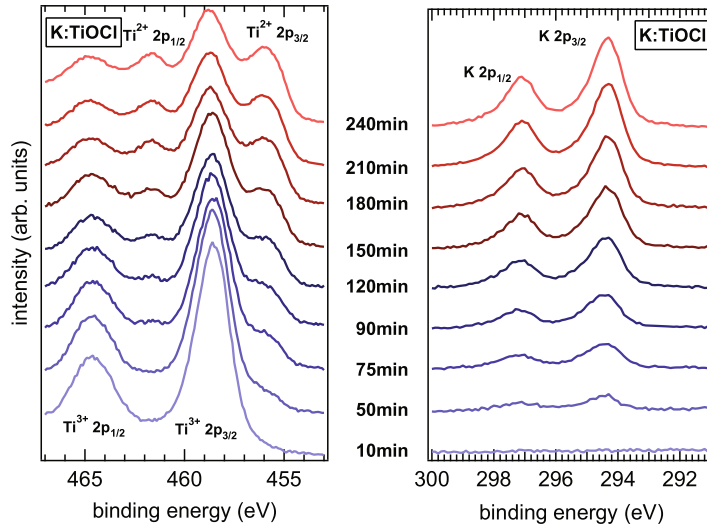


Fig. 4. (a) $Ti 2p$ and (b) $K 2p$ XPS spectra for various K vapor dosing times. The increasing Ti^{2+} -related weight is direct evidence for successful doping into the $Ti 3d$ shell.

intercalate) and that (ii) no structural or chemical modification occurs e.g. by the formation of $Na(K)Cl$ or alkali-metal oxides [21].

It can be inferred from the low-energy electron diffraction (LEED) patterns in Fig. 3(a) and (b) that the atomic long-range order is preserved up to significant doping concentrations. The pattern (b) for doped TiOCl ($x \approx 0.2$) neither displays additional superstructure spots, nor are the spots significantly broadened. Only a slight increase of diffuse scattering is observable. The chemical inertness of the oxyhalide host crystal is demonstrated by the unchanged $O 1s$ core level spectra depicted in Fig. 3(c) (except for a position shift due to the jump of the chemical potential, see below). Any marked change in the chemical bonding upon alkali-metal doping would be reflected in a change in line shape e.g. by an asymmetry, a broadening or additional features like shoulders or maxima. This is not seen here, and the same holds for all other core levels (not shown).

In Fig. 4(a) and (b) we show XPS spectra of the $Ti 2p$ and the $K 2p$ core levels with increasing dosing time, respectively. Clearly, the K content increases with dosing time. What is also seen is that at the lower binding energy side of each spin-orbit split $Ti 2p$ component additional spectral weight appears which grows concomitant with the K content. This can be readily ascribed to the $2p$ emission of Ti ions in the oxidation state 2+ (instead of 3+ for the pristine material), i.e. with an extra electron in the $Ti 3d$ shell. Due to the additional charge the effective core

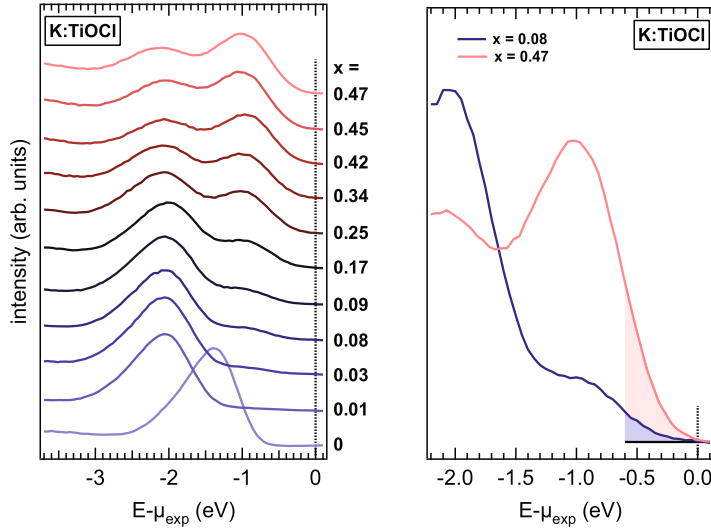


Fig. 5. Evolution of the Ti 3d spectral weight near the chemical potential as a function of doping x (left panel) and comparison of two magnified spectra at low and high doping to bring out the development of a soft gap more clearly (shaded areas in the right panel).

potential is better screened and hence the energy levels are shifted to lower binding energies. A quantitative analysis of the integral $Ti^{2+} 2p$ and $K 2p$ intensities, taking into account the relative photoionization cross sections, further reveals that essentially every K atom dopes one electron in the Ti 3d states.

Moreover, from the separate evaluation of the Ti^{2+} and the Ti^{3+} weight the doping concentration x can be determined – with no need of tabulated cross sections and hence very accurately – through $x = A(2+)/A(2+) + A(3+)$, where A denotes the corresponding peak areas.

In the angle-integrated UPS spectra of the valence band (see Fig. 5, left panel), the successful doping manifests itself in additional spectral weight, piling up with increasing doping concentration x near the chemical potential μ_{exp} [23]. Already after a tiny amount of doping, when almost no additional spectral weight is discernible yet, the whole spectrum shifts by about 0.6 eV to higher binding energies. At low x , a gap persists which gradually vanishes at higher doping. In the most simple picture of a Mott insulator the abrupt shift corresponds to a jump of the chemical potential from the midgap position to the lower edge of the upper Hubbard band (UHB) [4]. Note that the observed value of 0.6 eV is much smaller than half the optical gap of undoped TiOCl, which is ≈ 2 eV. In addition, with further doping one would expect the formation of a coherent quasiparticle peak at the chemical potential concomitant with a decrease of the lower Hubbard band (LHB) spectral weight, indicating a strongly correlated metallic state [24]. Instead, the doping-induced spectral weight develops in a broad hump, partly overlapping with the original spectral weight of the LHB. In particular, we point out that at higher doping levels the gap “softens” (see Fig. 5, right panel) with a power-law-like decrease of the spectral weight towards the chemical potential. This finding is in contrast to GGA + U calculations [26], which show a robust charge gap of ~ 1 eV for all doping concentrations up to $x = 1$. If one normalizes the integral 3d part of the spectra to $1 + x$ in accordance with the conservation of spectral weight, one finds that the doping-induced weight apparently grows at the expense of the LHB. A closer inspection shows that the LHB spectral weight decreases as $1 - x$ while the weight of the additional band increases as $2x$ (see Fig. 6(a) for K intercalation). This spectral weight transfer matches the expectation for the behavior of two correlated bands, e.g., the LHB and UHB of a Mott insulator in the atomic limit [25]. For each additional electron in the Ti 3d states, one possibility to remove an electron from a singly occupied Ti site at an orbital energy ε is lost in favor of two possibilities to remove an electron from a doubly occupied site at an energy $\varepsilon + U$.

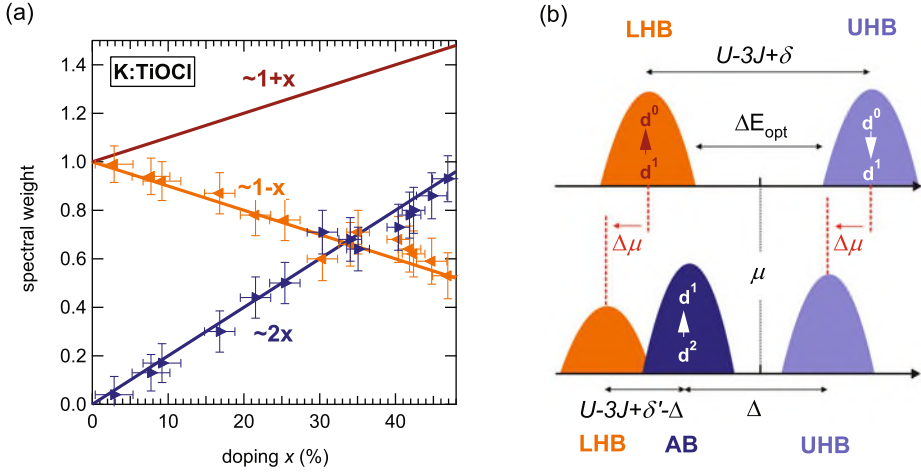


Fig. 6. (a) Total $3d$ spectral weight as a function of electron doping concentration x and decomposition into the weights related to the original and the doping induced spectral weight. The total spectral weight is normalized to $1+x$. (b) Sketch of the spectral weight distribution for $\text{TiOCl}(\text{Br})$ in the undoped and doped case. For details see text.

The above key observations, spectral weight transfer and absence of a metallic quasiparticle peak at the chemical potential, can be reconciled in an alloy or ionic Hubbard model type of scenario (cf. Fig. 6(b)). The salient point is that alkali-metal intercalation does not only yield to electron doping, rather the remaining ions which occupy specific cage positions close to certain Ti ions [26] give rise to point charge Coulomb potentials. These are strongest at these next Ti sites and average out for the ones farther away. As a result the intercalated alkali metal ions create a second kind of Ti sites with orbital energies lowered by Δ , the alloy sites. The states associated with the alloy sites form a band (alloy band, AB) in the gap between LHB and UHB. Thus, there is a finite excitation gap between AB and UHB and the material remains insulating at all doping levels. In a multiorbital picture of the oxyhalides the interaction energy for two electrons in the d shell is $U-3J$ due to the gain in exchange energy, if two different orbitals with parallel spin alignment are occupied. In addition, one has to take into account a small crystal field splitting of the two lowest-lying orbitals for the doped and undoped case (which might be slightly different [26]), δ and δ' . Then, one can arrive at the expressions given in Fig. 6(b) for the energies of the AB and UHB with respect to the LHB. Assuming reasonable values for all these parameters the energy separation of the LHB and the AB as well as the abrupt shift of the chemical potential can be consistently reconciled [27].

Finally, we comment on the apparent discrepancy regarding the gap behavior between experiment and theory. While in the density-functional calculations a robust charge gap of ~ 1 eV persists for all doping concentrations [26], in the PES data a distinct gap is seen only for doping levels up to $x \approx 0.2$. Beyond, a soft gap behavior is observed with a power-law-like suppression of spectral weight towards the chemical potential. We point out that even the inclusion of dynamical and spatial correlations as in dynamical mean-field theory most likely could not explain these observations, although it would take better into account the overall spectral lineshapes [28,29]. Rather this observation, may be related to recent reports on soft Hubbard gaps in the spectral function of an Anderson-Hubbard Hamiltonian. For it is well conceivable that the above picture of an alloy Hubbard model has to be qualified for the real material under study such that additional disorder is introduced in the AB at higher doping-levels. One could speculate that at low doping concentrations over distances smaller than the average dopant-dopant distance the electrostatic and structural perturbations are effectively screened and relaxed, respectively. With increasing doping the perturbations start to mutually affect each other but not necessarily in a cooperative manner since a periodic arrangement of the intercalants as perturbation centers might be hindered kinetically. Thus additional disorder might be introduced at the alloy sites. The use of larger alkali-metals such as Cs or organic

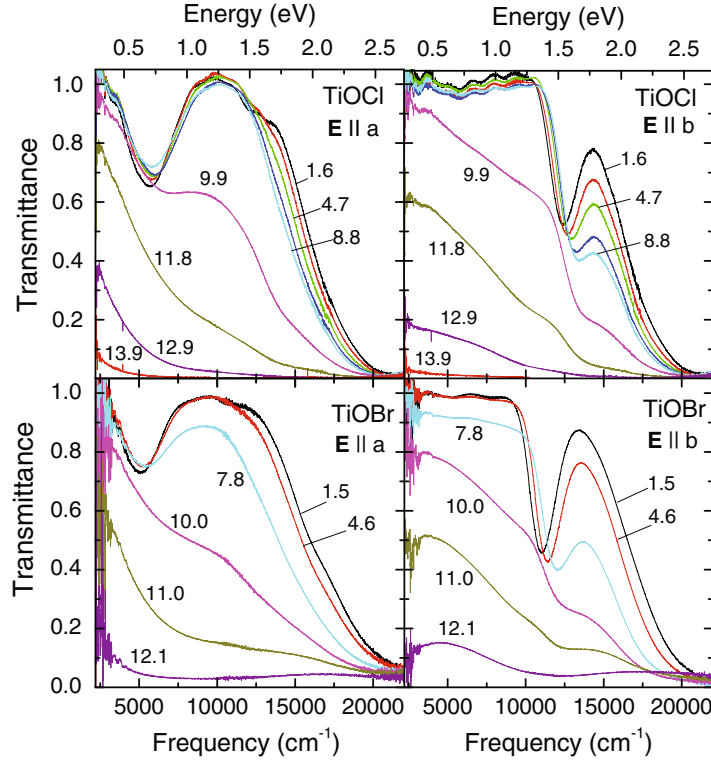


Fig. 7. Pressure-dependent transmittance spectra of TiOCl and TiOBr for $\mathbf{E}||a$ and $\mathbf{E}||b$ at room temperature (pressure medium: CsI). Numbers denote the applied pressures in GPa.

donor molecules as well as divalent alkaline earth metals offers the perspective to tune the strength of disorder and band filling and thereby to study systematically the phase diagram of correlated electron systems in the presence of disorder.

4.2 Effects of pressure

The possibility of a bandwidth-controlled MIT in the studied low-dimensional oxyhalides via the application of external pressure was probed by infrared spectroscopy. As demonstrated recently [30–32], the pressure technique combined with infrared spectroscopy is a powerful tool to characterize the pressure-induced MIT and the deconfinement transition in highly correlated materials on a quantitative level. The combined results of the pressure-dependent transmittance measurements on TiOCl and TiOBr are depicted in Fig. 7 [33–36]. The two measured polarization directions ($\mathbf{E}||a$, $\mathbf{E}||b$) lie parallel to the buckled Ti-O bilayers (see Fig. 1(b)). At low pressures, one observes absorption due to excitations across the crystal-field split Ti 3d energy levels located for TiOCl(Br) at 0.66 eV (0.63 eV) for $\mathbf{E}||a$ and at 1.53 eV (1.35 eV) for $\mathbf{E}||b$. Above ≈ 2 eV the transmittance is suppressed due to excitations across the Mott-Hubbard gap.

With increasing pressure, the orbital excitations exhibit a blueshift (see Fig. 7) which indicates an enhancement of the crystal field splitting under pressure. The most drastic change is a shift of the absorption edge due to excitations across the charge gap to smaller energies, and above 12 GPa (11 GPa) the overall transmittance is suppressed in TiOCl(Br). These results were obtained with CsI as pressure medium; for a more hydrostatic pressure medium like argon the transition pressure is higher ($\Delta p \approx 3$ GPa). The suppression of the transmittance at high pressures suggests the filling of the Mott-Hubbard gap with spectral weight, corresponding to excitations in the infrared frequency range. These additional excitations are directly observed in the real part of the optical conductivity, obtained by fitting the high-pressure reflectance

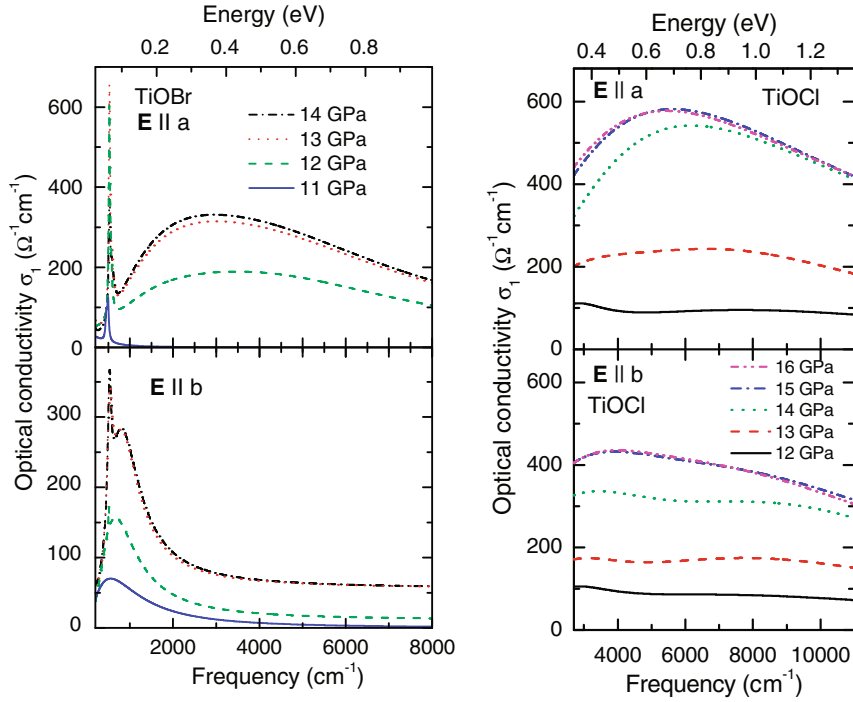


Fig. 8. Pressure-dependent real part of the optical conductivity of TiOBr and TiOCl for the polarization directions $\mathbf{E}||a$ and $\mathbf{E}||b$ at room temperature.

spectra (not shown) with the Drude-Lorentz model [35]. In Fig. 8 we present the optical conductivity spectra for both studied compounds. The main feature in the spectra is an absorption band located at a few 100 meV. The position of the absorption band depends on the polarization of the incident radiation. With increasing pressure the spectral weight of the absorption band increases and saturates [35]. For TiOCl the pressure-induced effects occur at slightly higher pressure ($\Delta p \approx 2$ GPa) compared to TiOBr. The extended low-frequency range for the conductivity spectrum of TiOBr shows a finite but small spectral weight in the far-infrared range, besides a sharp phonon features. This suggests that TiOBr (and in analogy TiOCl) most probably is in a metal-like state at high pressures (see the discussion below). However, the existence of a Drude contribution cannot unambiguously be proven based on the presented data.

The pressure-induced changes in the optical response coincide with a structural phase transition. The powder X-ray diffraction diagrams of TiOCl for selected pressures up to ~ 21.5 GPa are presented in Fig. 9. Up to the critical pressure $p_c \approx 15$ GPa the diffraction diagrams can be well described by LeBail fits applying symmetry and lattice parameters of the ambient-pressure, orthorhombic crystal structure (space group $Pmmn$). The lattice parameters and unit cell volume obtained by the LeBail fits are shown in Fig. 10 and are in agreement with those reported in Refs. [35,36]. We find a slightly nonlinear decrease of the lattice parameters with increasing pressure. Above $p_c \approx 15$ GPa the diffraction diagrams can no longer be described by a single phase, but a good fit of the data can only be achieved by assuming the coexistence of two phases – namely an orthorhombic phase (space group $Pmmn$) and a monoclinic phase (space group $P2_1/m$). The coexistence of two phases extends over a broad pressure range and signals the sluggish character of the structural phase transition. A large pressure range of phase coexistence, of 10 GPa or larger, has been observed for several first-order structural phase transitions [15,37,38] and suggests that the two phases are almost energetically degenerate. The monoclinic phase shows a doubling of the unit cell along the b axis with respect to the low-pressure orthorhombic phase (Fig. 10), in agreement with earlier reports [39]. Analogous results are obtained for TiOBr.

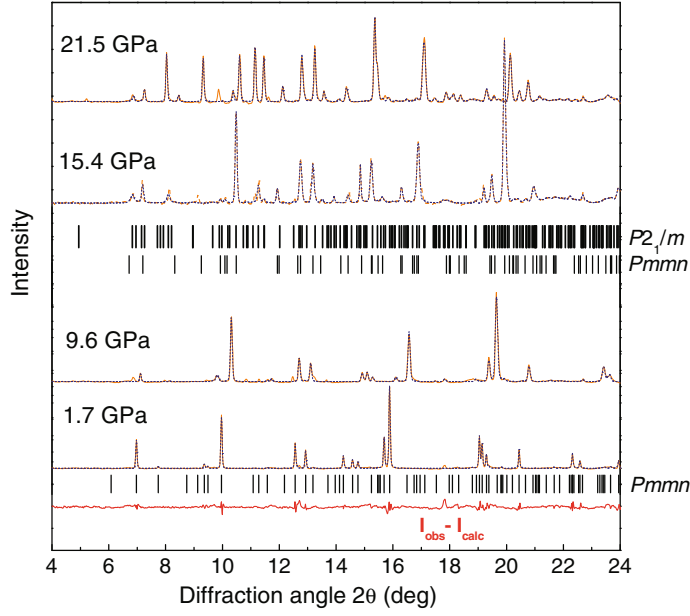


Fig. 9. Room-temperature X-ray powder diffraction diagrams of TiOCl at high pressures together with the LeBail fits (pressure medium: helium). For the lowest pressure (1.7 GPa) the difference curve ($I_{obs} - I_{calc}$) between the diffraction diagram and the LeBail fit is presented. Markers show the calculated peak positions for the various phases.

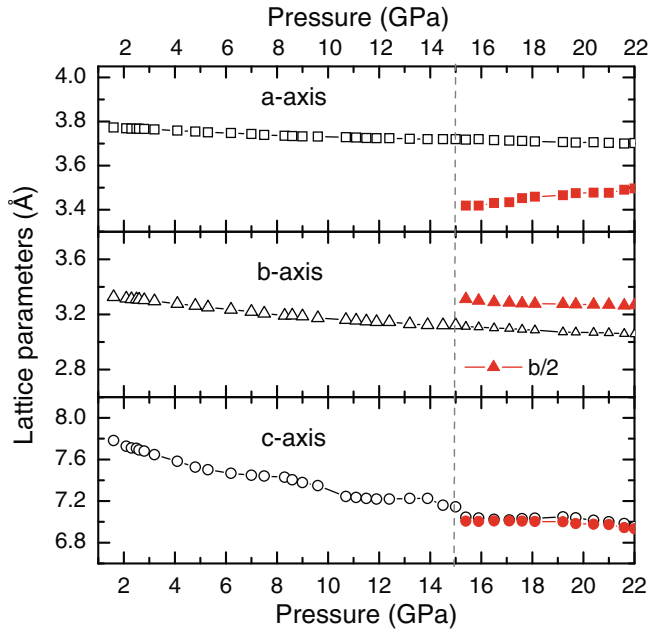


Fig. 10. Results of the LeBail fits of the room-temperature X-ray diffraction diagrams of TiOCl: lattice parameters as a function of pressure ($Pmmn$: black, open symbols; $P2_1/m$: red, full symbols). Lines are guides to the eye.

According to our experimental results [33–36], the charge gap in TiOCl and TiOBr is filled above a critical pressure with spectral weight located close to the Fermi energy. The appearance of additional spectral weight happens abruptly, which can be explained by the concomitant first-order structural phase transition. Whether or not itineracy of the charge carriers is reached in TiOCl(Br), is still debated. According to the optical data, there is a finite but small spectral

weight at low frequencies. However, the optical conductivity cannot unambiguously be fitted with a Drude term, the signature of coherent transport. The absence of coherent transport in a correlated system located on the metallic side of the Mott transition is not surprising: Optical conductivity spectra for different interaction strengths and different temperatures were obtained in a dynamical mean-field theory treatment of the Hubbard model [40]. It was shown that only below a certain temperature T_{coh} a quasiparticle peak involving coherent excitations appears at the Fermi energy and the Fermi liquid description applies. As a result, only at low temperatures ($T < T_{coh}$) a Drude term should be present in the optical conductivity spectrum. With increasing temperature, the quasiparticle peak is gradually destroyed and disappears above the temperature T_{coh} . Besides, it is known that in the close vicinity to the MIT line the charge carriers become easily localized due to extrinsic forces such as disorder and electron-lattice coupling. It was indeed suggested recently that the electron-lattice coupling in TiOCl is important and might trigger a conventional Peierls transition [39, 41].

The pressure-induced metallization of TiOCl and TiOBr is heavily debated. *Ab initio* molecular dynamics studies by Zhang et al. [42] predict for TiOCl a pressure-induced MIT with concomitant major structural changes. In contrast, according to the work of Blanco-Canosa et al. [39] an insulating and dimerized Peierls phase is expected above a critical pressure. This latter scenario is supported by electrical transport measurements on a TiOCl polycrystalline sample [43], which find a finite charge gap for all pressures up to 25 GPa: A decrease of the charge gap with increasing pressure was observed, which becomes less prominent for $P > 15$ GPa and approaches the value 0.15 eV at 25 GPa [43]. It is, however, clear that the quality of the contacts and the transport across grain boundaries in a polycrystalline sample might influence the experimental results. Transport measurements on single crystals along the *ab* plane are desirable, but the first issue (contact quality) would still remain to be considered. Contactless methods such as reflectivity measurements are advantageous in this regard, but they can suffer from diffraction effects limiting the lowest accessible frequency.

As mentioned above, the pressure-induced changes in the electronic properties of TiOCl and TiOBr are strongly coupled to the lattice degree of freedom. In particular, a key issue for the understanding of the physics of TiOCl and TiOBr might be the dimensionality of the systems determined by the underlying lattice. Early it was assumed that TiOCl can be described as a quasi-one-dimensional (quasi-1D) system, the main magnetic exchange interaction being the direct exchange between the spins along the *b* direction [6]. This picture could well explain the high-temperature susceptibility in terms of the 1D spin = 1/2 antiferromagnetic Heisenberg model with rather high nearest-neighbor exchange constants *J* of ~ 660 K and 375 K for TiOCl and TiOBr, respectively [6, 44, 45], but not the appearance of an incommensurate phase at intermediate temperatures, i.e., above the spin-Peierls transition temperature. A consistent picture was obtained by theoretical investigations and X-ray diffraction studies in a magnetic field which proposed that the ground state of TiOCl is determined by the interplay between the antiferromagnetic intrachain interaction and the frustrated, ferromagnetic interchain interaction [42, 46], and that it is better to be described as being close to two-dimensional, as already proposed in Refs. [9, 47, 48].

External pressure is an ideal tool to tune the atomic distances and hence directly influence the dimensionality of a system. As an illustration for the dimensionality change upon pressure application, we show in Fig. 11 the ratio of the lattice parameters *b* and *a* as a function of pressure for TiOCl, as obtained from the analysis of the X-ray diffraction data. Hereby we assume that the Ti-Ti distances scale with the lattice parameters. For the orthorhombic phase the ratio *b/a* monotonically decreases, and hence deviates stronger from 1, with increasing pressure, suggesting a pressure-induced enhancement of the 1D character of the system consistent with earlier reports [39]. The enhanced 1D character under pressure is due to the larger compressibility of the lattice along the *b* direction [39]. Thus, for $p < p_c$ pressure mainly changes the characteristics of the chains, with only a minor influence on the distance between them. At p_c the monoclinic phase with doubled unit cell along *b* is energetically degenerate with the orthorhombic phase. For the monoclinic phase the difference between the short and long Ti-Ti distances along *b* reaches a high value ($\approx 20\%$), and furthermore, the short Ti-Ti distance approaches the critical distance for metallic bonding [39]. Interestingly, for the monoclinic phase the ratio $(b/2)/a$ is close to one, i.e., the system is close to two-dimensional, for pressures close to p_c . This is due

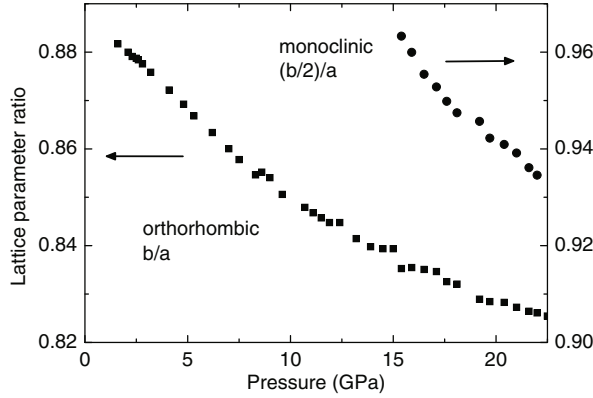


Fig. 11. Ratio of lattice parameters in the orthorhombic and monoclinic phases for TiOCl.

to the significant shrinkage (enlargement) of the unit cell along the a (b) direction compared to the orthorhombic phase (see Fig. 10). The interchain interaction is therefore expected to play an important role in the high-pressure monoclinic phase. With increasing pressure the lattice parameter ratio $(b/2)/a$ decreases slightly, signalling a small enhancement of the 1D character under pressure.

5 Summary

In summary, both doping and pressure lead to drastic changes in the electronic properties of the low-dimensional Mott-Hubbard insulators TiOCl and TiOBr. According to the spectral weight evolution upon alkali-metal doping electrons are doped into the Ti $3d$ states, but surprisingly a (soft) Coulomb gap persists. These findings are at variance with expectations within usual Mott-Hubbard scenarios, but can be reconciled if alkali-metal intercalated TiOCl(Br) is considered an alloy Mott insulator, where the alloy sites with changed orbital energies are induced electrostatically by the intercalants. Additional disorder at the alloy sites may be the reason for the observed peculiar soft gap behavior at higher electron doping concentrations.

Pressure application leads to the appearance of spectral weight close to the Fermi energy, and thus to a closure of the Mott-Hubbard gap. Simultaneously with the pressure-induced changes in the electronic properties a structural phase transition occurs. We do not find clear evidence for coherent transport in the high-pressure phase, at least at room temperature. The absence of a coherent quasi-particle peak could be explained within the Hubbard model, which predicts coherent transport only below a certain temperature and not too close to the MIT line. We propose that the system's dimensionality, which can be directly tuned by external pressure, is one of the key aspects for an understanding of the unusual electronic and magnetic properties of TiOCl and TiOBr.

We acknowledge the ANKA Angströmquelle Karlsruhe for the provision of beamtime and we would like to thank B. Gasharova, Y.-L. Mathis, D. Moss, and M. Stüpfle for assistance using the beamline ANKA-IR. Facilities and beamtime provided by the European Synchrotron Radiation Facility is gratefully acknowledged. We are grateful to T. Demarczyk for growing high-quality crystals in Würzburg. Financial support by the DFG, including the Emmy Noether-program, SFB 484, and CL124/6-1, is acknowledged.

References

1. N.F. Mott, Proc. Phys. Soc. London Sect. A **62**, 416 (1949)
2. P.W. Anderson, Phys. Rev. **109**, 1492 (1958)

3. H. Shinaoka, M. Imada, *Phys. Rev. Lett.* **102**, 016404 (2009)
4. M. Imada, A. Fujimori, Y. Tokura, *Rev. Mod. Phys.* **70**, 1039 (1998)
5. H. Schäfer, F. Wartenpfehl, E. Weise, *Z. Anorg. Allg. Chem.* **295**, 268 (1958)
6. A. Seidel, C.A. Marianetti, F.C. Chou, G. Ceder, P.A. Lee, *Phys. Rev. B* **67**, 020405(R) (2003)
7. P. Lemmens, K.Y. Choi, R. Valentí, T. Saha-Dasgupta, E. Abel, Y.S. Lee, F.C. Chou, *New J. Phys.* **7**, 74 (2005)
8. P.W. Anderson, *Mater. Res. Bull.* **8**, 153 (1973)
9. R.J. Beynon, J.A. Wilson, *J. Phys.: Condens. Matter* **5**, 1983 (1993)
10. H. Schäfer, *Chemische Transportreaktionen* (Verlag Chemie, Weinheim, 1962)
11. R. Nitzsche, *Fortschritte der Mineralogie* **44**, 231 (1967)
12. L. Palatinus, A. Schönleber, S. van Smaalen, *Acta Cryst., Section C* **61**, i48 (2005)
13. G. Huber, K. Syassen, W.B. Holzapfel, *Phys. Rev. B* **15**, 5123 (1977)
14. H.K. Mao, J. Xu, P.M. Bell, *J. Geophys. Res.* **91**, 4673 (1986)
15. I. Loa, K. Syassen, X. Wang, F. Lichtenberg, M. Hanfland, C.A. Kuntscher, *Phys. Rev. B* **69**, 224105 (2004)
16. S. Frank, C.A. Kuntscher, I. Loa, K. Syassen, F. Lichtenberg, *Phys. Rev. B* **74**, 054105 (2006)
17. M.I. Eremets, Y.A. Timofeev, *Rev. Scient. Instrum.* **63**, 3123 (1992)
18. A.L. Ruoff, K. Ghandehari, in S.C. Schmidt, J.W. Shaner, G.A. Samara, M. Ross (eds.), *High Pressure Science and Technology*, pp. 1523-1525, *American Institute of Physics Conference Proceedings 309* (Woodbury, N.Y., 1994)
19. A. Hammersley, *Computer Program FIT2D* (ESRF, Grenoble, 1998)
20. V. Petricek, M. Dusek, L. Palatinus, *Jana2006, A Crystallographic Computing System* (Institute of Physics, Praha, Czech Republic 2006)
21. S. Yamanaka, T. Yasunaga, K. Yamaguchi, M. Tagawa, *J. Mater. Chem.* **19**, 2573 (2009)
22. M.A. Hossain, J.D.F. Mottershead, D. Fournier, A. Bostwick, J.L. McChesney, E. Rotenberg, R. Liang, W.N. Hardy, G.A. Sawatzky, *Nat. Phys.* **4**, 527 (2008)
23. The chemical potential is referenced to the Fermi edge of a Ag foil. Since the samples charge up in PES, obeying activated behavior, the energy axis was determined by extrapolating a temperature dependent series of spectra to zero charging. We denote the thus determined position of the chemical potential by μ_{exp}
24. H. Kajueter, G. Kotliar, G. Moeller, *Phys. Rev. B* **53**, 16214 (1996)
25. H. Eskes, M.B.J. Meinders, G.A. Sawatzky, *Phys. Rev. Lett.* **67**, 1035 (1991)
26. Y.Z. Zhang, K. Foyevtsova, H.O. Jeschke, M.U. Schmidt, R. Valentí [[arXiv:0905.1276](https://arxiv.org/abs/0905.1276)]
27. M. Sing, S. Glawion, M. Schlachter, M.R. Scholz, K. Goss, J. Heidler, G. Berner, R. Claessen [[arXiv:0905.1381v2](https://arxiv.org/abs/0905.1381v2)]
28. M. Hoinkis, M. Sing, J. Schäfer, M. Klemm, S. Horn, H. Benthien, E. Jeckelmann, T. Saha-Dasgupta, L. Pisani, R. Valentí, *Phys. Rev. B* **72**, 125127 (2005)
29. T. Saha-Dasgupta, A. Lichtenstein, M. Hoinkis, S. Glawion, M. Sing, R. Claessen, R. Valentí, *New J. Phys.* **9**, 380 (2007)
30. J. Kuneš, L. Baldassarre, B. Schächner, K. Rabia, C.A. Kuntscher, Dm. M. Korotin, V.I. Anisimov, J.A. McLeod, E.Z. Kurmaev, A. Moewes, *Phys. Rev. B* **81**, 035122 (2010)
31. A. Pashkin, M. Dressel, C.A. Kuntscher, *Phys. Rev. B* **74**, 165118 (2006)
32. A. Pashkin, M. Dressel, M. Hanfland, C.A. Kuntscher, *Phys. Rev. B* **81**, 125109 (2010)
33. C.A. Kuntscher, S. Frank, A. Pashkin, M. Hoinkis, M. Klemm, M. Sing, S. Horn, R. Claessen, *Phys. Rev. B* **74**, 184402 (2006)
34. C.A. Kuntscher, S. Frank, A. Pashkin, H. Hoffmann, A. Schönleber, S. van Smaalen, M. Hanfland, S. Glawion, M. Klemm, M. Sing, S. Horn, R. Claessen, *Phys. Rev. B* **76**, 241101(R) (2007)
35. C.A. Kuntscher, A. Pashkin, H. Hoffmann, S. Frank, M. Klemm, S. Horn, A. Schönleber, S. van Smaalen, M. Hanfland, S. Glawion, M. Sing, R. Claessen, *Phys. Rev. B* **78**, 035106 (2008)
36. C.A. Kuntscher, J. Ebad-Allah, A. Pashkin, S. Frank, M. Klemm, S. Horn, A. Schönleber, S. van Smaalen, M. Hanfland, S. Glawion, M. Sing, R. Claessen, *High Pressure Res.* **29**, 509 (2009)
37. G.Kh. Rozenberg, M.P. Pasternak, P. Gorodetsky, W.M. Xu, L.S. Dubrovinsky, T. Le Bihan, R.D. Taylor, *Phys. Rev. B* **79**, 214105 (2009)
38. W.M. Xu, O. Naaman, G.Kh. Rozenberg, M.P. Pasternak, R.D. Taylor, *Phys. Rev. B* **64**, 094411 (2001)
39. S. Blanco-Canosa, F. Rivadulla, A. Pineira, V. Pardo, D. Baldomir, D.I. Khomskii, M.M. Abd-Elmeguid, M.A. Lopez-Qintela, J. Rivas, *Phys. Rev. Lett.* **102**, 056406 (2009)
40. A. Georges, G. Kotliar, W. Krauth, M.J. Rozenberg, *Rev. Mod. Phys.* **68**, 13 (1996)

41. A. Prodi, J.S. Helton, Y. Feng, Y.S. Lee [[arXiv: 0908.0518](#)]
42. Y.-Z. Zhang, H.O. Jeschke, R. Valenti, *Phys. Rev. Lett.* **101**, 136406 (2008)
43. M.K. Forthaus, T. Taetz, A. Möller, M.M. Abd-Elmeguid, *Phys. Rev. B* **77**, 165121 (2008)
44. T. Sasaki, M. Mizumaki, T. Nagai, T. Asaka, K. Kato, M. Takata, Y. Matsui, J. Akimitsu, *J. Phys. Soc. Jpn.* **74**, 2185 (2005)
45. C. Kato, Y. Kobayashi, M. Sato, **74**, 473 (2005)
46. A. Krimmel, J. Strepfer, B. Bohnenbuck, B. Keimer, M. Hoinkis, M. Klemm, S. Horn, A. Loidl, M. Sing, R. Claessen, M.V. Zimmermann, *Phys. Rev. B* **73**, 172413 (2006)
47. R. Rückamp, J. Baier, M. Kriener, M.W. Haverkort, T. Lorenz, G.S. Uhrig, L. Jongen, A. Möller, G. Meyer, M. Grüninger, *Phys. Rev. Lett.* **95**, 097203 (2005)
48. M. Hoinkis, M. Sing, S. Glawion, L. Pisani, R. Valentí, S. van Smaalen, M. Klemm, S. Horn, R. Claessen, *Phys. Rev. B* **75**, 245124 (2007)